

Study of Lithium Dynamics in Monoclinic $\text{Li}_3\text{Fe}_2(\text{PO}_4)_3$ using ^6Li VT and 2D Exchange MAS NMR Spectroscopy[†]

L. J. M. Davis,[‡] I. Heinmaa,[§] and G. R. Goward^{*‡}

[‡]Department of Chemistry and Brockhouse Institute for Materials Research, McMaster University, 1280 Main Street West, Hamilton, Ontario, L8S 4M1 Canada, and [§]National Institute of Chemical Physics and Biophysics, Akadeemia tee 23, 12618 Tallinn, Estonia

Received May 22, 2009. Revised Manuscript Received August 20, 2009

Details of Li-mobility in $\text{Li}_3\text{Fe}_2(\text{PO}_4)_3$ are elucidated using solid-state ^6Li NMR. Three crystallographically unique Li sites were resolved under magic angle spinning (25 kHz) with paramagnetic shifts arising at 45 ppm, 102 ppm, and 216 ppm. These resonances were assigned to the crystallographic positions based on the degree of the Fermi-contact interaction with the paramagnetic iron center. ^6Li 2D exchange NMR experiments were performed under variable temperature conditions in order to determine the activation energies for hopping between lithium sites. Activation energies ranged from 0.59 (\pm 0.05) eV to 0.81 (\pm 0.04) eV, where shorter Li internuclear distances and larger Li–O bottlenecks yielded lower activation energies. These results were compared to a previous study on the isostructural $\text{Li}_3\text{V}_2(\text{PO}_4)_3$, which showed similar trends of increased internuclear distance (and constricted bottlenecks) yielding larger energy barriers for Li–Li exchange. Overall, the average activation energy for lithium ion hopping in the iron-based structure is lower than the vanadium analogue, which is attributed to the more open framework of the former.

Introduction

Many members of the phosphate family of cathode materials for Li-ion batteries have been studied extensively.¹ Despite this, there is a notable absence of dynamics information regarding the mobile Li-ion. Powder X-ray diffraction, as well as a variety of spectroscopic techniques can provide useful information about structural changes to the lattice taking place during electrochemical cycling. Solid-state ^6Li nuclear magnetic resonance (NMR) studies can provide time scales and activation energies for Li-ion mobility that provide structure–function correlations that are essential for the development of safe and efficient Li-ion batteries.

The high cost and toxicity of the widely used cathode material, LiCoO_2 , has motivated widespread investigation into alternative cathodes. Although some researchers have focused on other members of the Li-oxide family including LiMn_2O_4 ^{2,3} and $\text{LiCo}_{1/3}\text{Ni}_{1/3}\text{Mn}_{1/3}\text{O}_2$,⁴ Li-ion transition metal phosphates have emerged as strong candidates for use in Li-ion batteries. The phosphate materials demonstrate superior electrochemical and ther-

mal stability when undergoing electrochemical cycling as compared to their oxide analogues. This is largely attributed to the inductive effect created by the PO_4^{3-} tetrahedra, where the electron density of the oxygen atoms is polarized away from both the transition metal and mobile ion thus creating large channels for Li ions.⁵ This leads to materials with the promise of high Li-ion mobility coupled with structural stability. The iron phosphate family of materials including the olivine LiFePO_4 ,¹ NASICON $\text{Li}_3\text{Fe}_2(\text{PO}_4)_3$,⁶ and monoclinic $\text{Li}_3\text{Fe}_2(\text{PO}_4)_3$,^{5,7} have been an exceptional point of interest due to their low cost and low environmental impact. The appreciable redox potentials of the $\text{Fe}^{3+}/\text{Fe}^{2+}$ redox couple for these materials occur at approximately 3.43, 3.55, and 2.8 V vs Li-metal, respectively. Despite the advantages of using the iron phosphate materials, overall these compounds exhibit surprisingly poor electronic and ionic conductivity, which has limited their commercial success. Lithium NMR is well-known to be an in depth tool for studying structural and dynamic factors that influence poor electrochemical performance.^{8–11} Lithium in these materials is directly involved in the electrochemical process and, moreover, shows sensitivity to electronic changes that take place in the surrounding lattice during lithium

[†] Accepted as part of the 2010 “Materials Chemistry of Energy Conversion Special Issue”.

^{*}Corresponding author. Email: goward@mcmaster.ca. Phone: (905) 525-9140 ×24176. Fax: (905) 522-2509.

(1) Padhi, A. K.; Nanjundaswamy, K. S.; Goodenough, J. B. *J. Electrochem. Soc.* **1997**, *144*, 1188–1194.
(2) Thackeray, M. M. *J. Electrochem. Soc.* **1995**, *142*, 2558–2563.
(3) Tarascon, J. M.; Wang, E.; Shokoohi, F. K.; McKinnon, W. R.; Colson, S. J. *Electrochem. Soc.* **1991**, *138*, 2859–2864.
(4) Ohzuku, T.; Makimura, Y. *Chem. Lett.* **2001**, 642–643.
(5) Padhi, A. K.; Nanjundaswamy, K. S.; Masquelier, S.; Okada, S.; Goodenough, J. B. *J. Electrochem. Soc.* **1997**, *144*, 1609–1613.

(8) Cahill, L. S.; Chapman, R. P.; Britten, J. F.; Goward, G. R. *J. Phys. Chem. B* **2006**, *110*, 7171–7177.
(9) Grey, C. P.; Lee, Y. J. *Solid State Sci.* **2003**, *5*, 883–894.
(10) Cahill, L. S.; Kirby, C. W.; Goward, G. R. *J. Phys. Chem. C* **2008**, *112*, 2215–2221.
(11) Makimura, Y.; Cahill, L. S.; Iriyama, Y.; Goward, G. R.; Nazar, L. F. *Chem. Mater.* **2008**, *20*, 4240–4248.

extraction, making it an interesting nucleus for solid-state NMR studies.

The present study focuses on the Li-ion dynamics in the monoclinic $\text{Li}_3\text{Fe}_2(\text{PO}_4)_3$. This material crystallizes in a structure similar to the open framework NASICON structure with space group $\text{P2}_1/\text{n}$.¹² The structure is a three-dimensional framework of FeO_6 -octahedra and PO_4 -tetrahedra. There are three crystallographically unique Li sites where Li1 occupies the tetrahedral position and Li2 and Li3 both occupy the distorted trigonal bipyramidal sites. All three sites are resolved under fast magic angle spinning (MAS) in ^6Li 1D NMR spectra, where the paramagnetic shifts are initially assigned based on the extent of the Fermi-contact interaction between the Li and nearby paramagnetic iron center.

Both 1D and 2D variable-temperature MAS NMR experiments give information about time scales of Li^+ motion.^{8,13–17} Investigation of exchange between crystallographic Li sites is accomplished using two-dimensional exchange spectroscopy (2D EXSY).¹⁸ This technique has been applied previously to determine Li exchange in materials including LiMn_2O_4 ,¹⁶ $\text{Li}_3\text{V}_2(\text{PO}_4)_3$,⁸ and Li_4SiO_4 .¹⁹ EXSY experiments yield data that can be interpreted in the context of the structural constraints on lithium diffusion including time scales of lithium exchange and energy barriers to this diffusion as discussed in the context of Li-ion bottlenecks and Li–Li inter-nuclear distances. These results are compared to the 2D EXSY studies of structurally similar $\text{Li}_3\text{V}_2(\text{PO}_4)_3$.⁸

Experimental Section

Sample Preparation. $\text{Li}_3\text{Fe}_2(\text{PO}_4)_3$ was prepared by solid-state reaction as described by Padhi et al.⁵ Stoichiometric amounts of $\text{NH}_4\text{H}_2\text{PO}_4$ (Sigma Aldrich, 99%), $^6\text{LiOH}$ (prepared in house using Cambridge isotopes ^6Li metal), and Fe_2O_3 (Sigma Aldrich, 99%) were ground together and heated to 250 °C to drive off ammonia and water. The mixture was reground and fired again, this time bringing the sample to 850 °C over a period of 24 h and then holding for 2 days. The sample was reground, pelletized, and sintered at 930 °C for 24 h. Synthesized samples were characterized using a PANalytical diffractometer with $\text{Cu K}\alpha$ radiation ($\lambda = 1.5406 \text{ \AA}$). Data were collected from 10 to 90° in 2θ step size of 0.016 with a step time of 100 s. The reflections were indexed in agreement with the literature.¹²

Solid-State NMR. Room-temperature 1D ^6Li MAS NMR and 2D EXSY spectra were acquired at a Larmor frequency of

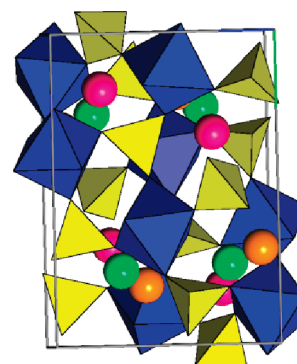


Figure 1. Unit cell of monoclinic $\text{Li}_3\text{Fe}_2(\text{PO}_4)_3$ along the a -axis. FeO_6 octahedra (blue) are connected to PO_4^{3-} tetrahedra (yellow) at oxygen vertices. Li1 (pink), Li2 (green) and Li3 (orange) sit in channels formed by the PO_4 and FeO_6 units.

29.4 MHz on a Bruker AMX 200 spectrometer. A custom-built double resonance probe supporting 1.8 mm rotors capable of MAS frequencies of 25 kHz up to 45 kHz was used. Temperatures were calibrated using $\text{Pb}(\text{NO}_3)_2$ as described elsewhere.²⁰ The spectra were referenced to 1 M $^6\text{LiCl}$ (aq) (0 ppm). ^6Li 1D spectra were acquired using a Hahn-echo pulse sequence with a 90° pulse of 2.5 μs and recycle delay of 50 ms. T_1 relaxation times were determined using a standard saturation recovery sequence. 2D exchange spectra were acquired using mixing times from 100 μs to 8 ms. The number of slices in the indirect dimension was 512. Phase-sensitive detection in t_1 was achieved through the use of States-TPPI.²¹

Impedance Spectroscopy. Impedance measurements were performed on $\text{Li}_3\text{Fe}_2(\text{PO}_4)_3$ using an AUTOLAB PGSTST30 frequency response analyzer. The instrument was used in potentiostatic mode with an AC potential amplitude of 0.5 V over a frequency range of 400 kHz to 0.1 Hz. The powder samples were pelletized and sintered at 850 °C for 12 h. The thickness of the pellets was measured by micrometer, and was $2.41 \pm 0.5 \text{ mm}$. Data were acquired over a temperature range of 300–350 K in steps of 10 K.

Results and Discussion

The three Li crystallographic positions of $\text{Li}_3\text{Fe}_2(\text{PO}_4)_3$ (Figure 1) were easily resolved in the 1D ^6Li NMR spectrum with MAS of 25 kHz (Figure 2). Resonances that arise at 45, 102, and 216 ppm are designated as sites A, B, and C, respectively. A preliminary assignment of the ^6Li resonances to the crystallographic positions was made on the basis of the geometry-dependent electron spin density transfer from the paramagnetic iron center to the Li and P atoms.^{8,22} There are two mechanisms for electron spin density transfer.^{9,23} This transfer is found to be most effective when the M–O–Li orbitals overlap at angles close to 90 or 180°. Because the monoclinic family of $\text{Li}_3\text{M}_2(\text{PO}_4)_3$ compounds have orbital overlap angles closer to 90°, the 180° interactions are neglected. The mechanism in Figure 3a shows the delocalization

- (12) Bykov, A. B.; Chirkin, A. P.; Demyants, L. N.; Doronin, S. N.; Genkin, E. A.; Ivanov-Shits, A. K.; Kondratyuk, I. P.; Maksimov, B. A.; Mel'kinov, O. K.; Muradyan, L. N.; Simonov, V. I.; Timofeeva, V. A. *Solid State Ionics* **1990**, *38*, 31–52.
- (13) Qi, F.; Jorg, T.; Bohmer, R. *Solid State Nucl. Magn. Reson.* **2002**, *22*, 484–500.
- (14) Wilkening, M.; Heitjans, P. *Phys. Rev B* **2008**, *77*, 024311 (1–13).
- (15) Wilkening, M.; Kuhn, A.; Heitjans, P., *Phys. Rev B* **2008**, *78*, 054303 (1–9).
- (16) Verhoeven, V. W. J.; de Schepper, I. M.; Nachtegaal, G.; Kentgens, A. P. M.; Kelder, E. M.; Schoonman, J.; Mulder, F. M. *Phys. Rev. Lett.* **2001**, *86*, 4314–4317.
- (17) Xu, Z.; Stebbins, J. F. *Science* **1995**, *270*, 1332–1334.
- (18) Jeener, J.; Meier, B. H.; Bachmann, P.; Ernst, R. R. *J. Chem. Phys.* **1979**, *71*, 4546–4553.
- (19) Xu, Z.; S., J. F. *Science* **1995**, *270*, 1332.

- (20) Takahashi, T.; Kawashima, H.; Sugisawa, H.; Baba, T. *Solid State Nucl. Magn. Reson.* **1999**, *15*, 119–123.
- (21) Marion, D.; Ikura, M.; Tschudin, R.; Bax, A. J. *Magn. Reson.* **1989**, *85*, 393–399.
- (22) Grey, C. P.; Dupree, N. *Chem. Rev.* **2004**, *104*, 4493–4512.
- (23) Ceder, G.; Chiang, Y. M.; Sadoway, D. R.; Aydinol, M. K.; Jang, Y. I.; Huang, B. *Nature* **1998**, *392*, 694–696.

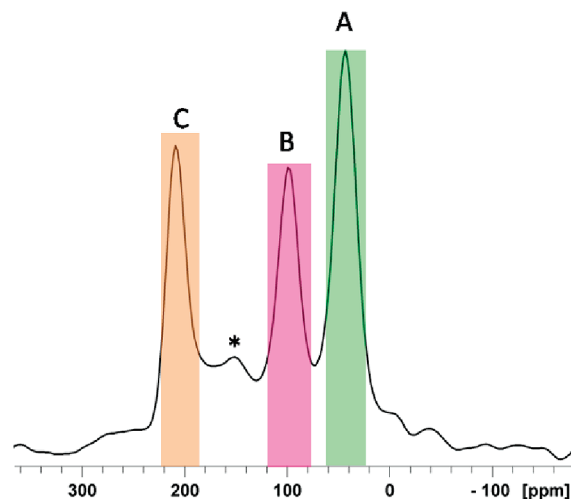


Figure 2. ^6Li MAS NMR spectrum of $\text{Li}_3\text{Fe}_2(\text{PO}_4)_3$ with MAS=25 kHz. Asterisk denotes peak belonging to impure phase.

mechanism where unpaired electron spin density from the Fe t_{2g} orbital is transferred to the empty Li 2s orbital either directly or via the O 2p orbital. This results in a transfer of electronic spin density where the sign of the spin is unchanged from that of the transition metal, leading to an increase in the nuclear chemical shift. Alternatively, Figure 3b shows the polarization mechanism where the electron spin density of the t_{2g} orbital is polarized by unpaired electrons sitting in the e_g orbital of the transition metal center. This increases the positive spin density at the transition metal center thus inducing negative spin density on the O 2p orbital which is then transferred to the empty Li 2s orbital. This leads to a decrease in the nuclear chemical shift. Overall, these interactions are additive and in general delocalization prevails more often than the polarization scheme.²² This also means the crystallographic data becomes essential when making the shift assignment as bond lengths and angles among M–O–Li interactions allow the prediction of the aforementioned mechanisms.

The assignment of the 1D ^6Li MAS NMR spectrum for $\text{Li}_3\text{Fe}_2(\text{PO}_4)_3$ was made in consideration of the previously assigned 1D ^7Li MAS NMR spectrum of the isostructural $\text{Li}_3\text{V}_2(\text{PO}_4)_3$.⁸ For ease of comparison, the labeling of Li2 and Li3 in this study is reversed from the work of Bykov et al.¹² in order to maintain consistency between the NMR study of $\text{Li}_3\text{V}_2(\text{PO}_4)_3$ that draws upon the labeling scheme of Yin et al.²⁴ Although the trends in chemical shifts are similar for the two materials, the magnitude of the shifts is larger for the iron compound studied here. First, the difference in electronic configuration of the Fe^{3+} and V^{3+} centers is noted in this comparative assignment. The V^{3+} center has an electron configuration of $t_{2g}^2 e_g^0$, where only the transfer of positive electron spin density from the t_{2g} orbital (via the 90° delocalization mechanism) contributes to the paramagnetic shift. The empty e_g orbital eliminates the possibility of spin polarization which would decrease the paramagnetic shift.

a) Delocalization Mechanism

b) Polarization Mechanism

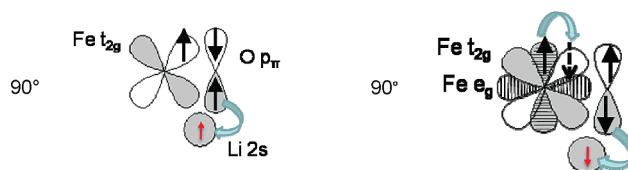


Figure 3. Schematic detailing two mechanisms for electron spin density transfer, styled after ref 18. (a) Delocalization of unpaired electron spin density from the Fe t_{2g} to the empty Li 2s orbital either directly or via the O 2p orbital. This leads to spin density being of the same sign as that on the Fe center. (b) Unpaired electron spin density in the e_g orbital (shown with hatching) polarizing spin in the t_{2g} orbital, thus leading to density transfer to the empty Li 2s orbital of opposite sign to that of the Fe center, which leads to a decrease in paramagnetic shift.

Table 1. Summary of Crystallographic Data for $\text{Li}_3\text{Fe}_2(\text{PO}_4)_3$

Li site	distance to Fe (Å)	Li–O–Fe angle (deg)
Li1	3.055	97.83
	3.055	98.22
	2.869	93.91
	2.869	92.45
Li3	3.033	102.6
	3.033	90.41
	2.872	85.03
	2.872	77.92
Li2	2.872	89.51
	3.589	111.96
	3.540	126.51
	2.742	83.43
	2.742	87.73
	2.742	72.18

Therefore the highest paramagnetic resonance (at 107 ppm) was assigned to the Li site with the highest number of V–O–Li angles close to 90° ($\pm 4^\circ$) and the lowest shift (17 ppm) assigned to the Li with the poorest V–O–Li overlap. It should be noted that the $^6/7\text{Li}$ chemical shift range in diamagnetic materials is on the order of ± 10 ppm, meaning the high chemical shift range for paramagnetic $\text{Li}_3\text{M}_2(\text{PO}_4)_3$ compounds is entirely due to the Fermi contact with the paramagnetic centers. For $\text{Li}_3\text{Fe}_2(\text{PO}_4)_3$, the Fe^{3+} has an electron configuration of high spin $t_{2g}^3 e_g^2$. As compared to the vanadium case, there is one more electron in the t_{2g} orbital capable of delocalizing positive spin density but now the e_g orbitals are able to polarize spin density and decrease the paramagnetic shift. Despite this fact, however, the overall chemical shift range for the three Li crystallographic sites of $\text{Li}_3\text{Fe}_2(\text{PO}_4)_3$ is significantly higher (45–216 ppm) than that of the vanadium analogue (17–107 ppm). This is consistent with the addition of one more unpaired electron in the t_{2g} orbitals and the assertion that the delocalization mechanism is often dominant over the polarization mechanism.²² The highest chemical shift, C, is assigned to Li3 which showed orbital interactions with the strongest 90° overlap (90.41° and 89.51°) (Table 1). The lowest resonance, A, at 45 ppm is assigned to Li2, which had the poorest Li–O–Fe overlap. Site B is therefore assigned to the four coordinate Li1 site, which has two sites close to 90° (93.91° and 92.45°). The assignment of the Li2 and Li3 crystallographic sites is

(24) Yin, S.-C.; Grodny, P.; Anne, M.; Nazar, L. F. *J. Am. Chem. Soc.* **2003**, *125*, 10402–10411.

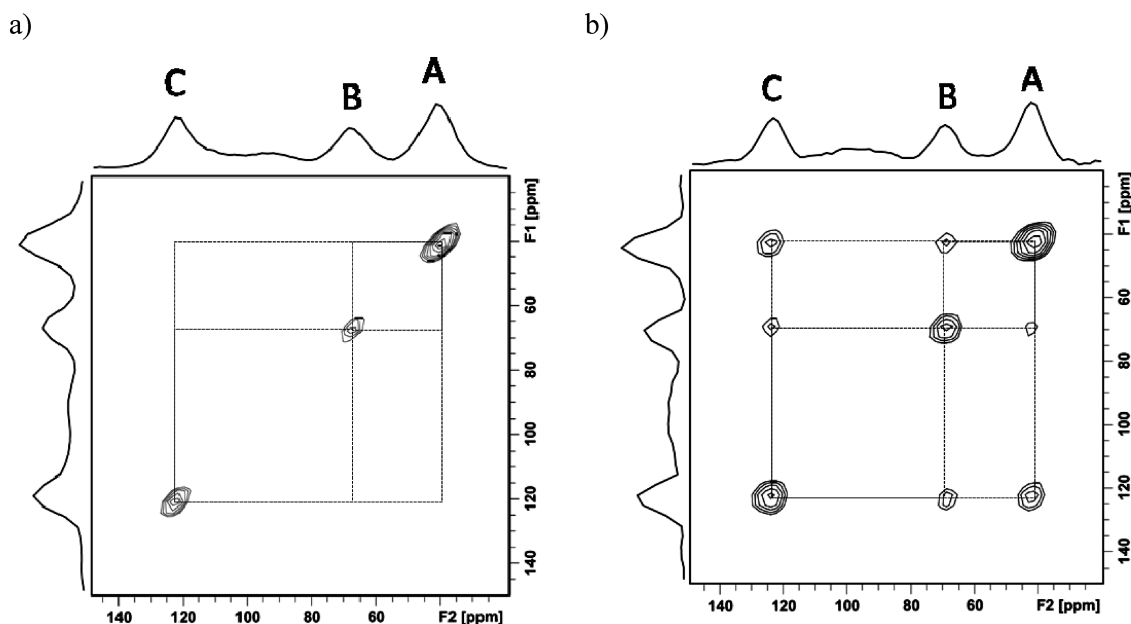


Figure 4. ^6Li 2D EXSY spectrum at MAS = 25 kHz, $T = 311$ K, with (a) $\tau_{\text{mix}} = 0.5$ ms and (b) $\tau_{\text{mix}} = 3.0$ ms.

opposite to that of $\text{Li}_3\text{V}_2(\text{PO}_4)_3$. This is attributed to a structural difference between the two, where the number of 90° interactions for Li2 and Li3 is reversed.²⁴

This assignment for the crystallographic Li sites in $\text{Li}_3\text{Fe}_2(\text{PO}_4)_3$ was supported by the 2D EXSY data where the correlation times and activation energies between exchange pairs relate well to the distance and bottleneck size between each exchange pair. In the 2D EXSY experiment, each spin is frequency-labeled during the evolution period, t_1 . The exchange processes are allowed to take place during the following mixing period of set length, τ_m . Through successive experiments, the integrated volume of the cross peaks plotted as a function of mixing time yields a correlation time for the exchange process. The mixing period is limited by the spin–lattice relaxation time (T_1) of the spins. The increased number of unpaired electrons had a profound effect on the T_1 times when comparing the Fe and V compounds. For $\text{Li}_3\text{V}_2(\text{PO}_4)_3$, ^7Li relaxation times for all three resonance were on the order of 6.0 ± 0.2 ms. For $\text{Li}_3\text{Fe}_2(\text{PO}_4)_3$, ^7Li T_1 times for all resonances were shortened significantly to 1.1 ± 0.2 ms because of the addition of 3 unpaired electrons and increased paramagnetic character of the Fe compound. To achieve a first-order exponential buildup to extract an accurate correlation time, mixing times longer than 1 ms were needed. A smaller quadrupole moment and lower magnetogyric ratio for ^6Li gives weaker dipolar coupling values than the ^7Li counterpart, resulting in longer T_1 relaxation values. Therefore, samples of $\text{Li}_3\text{Fe}_2(\text{PO}_4)_3$ were prepared with ^6Li -enriched LiOH, which increased T_1 times for all three sites to 8.0 ± 0.2 ms and allowed for longer mixing times to be used.

Figure 4 shows ^6Li 2D EXSY spectra acquired at 311 K. For shorter mixing times, exchange was not observed as seen in Figure 4a where $\tau_{\text{mix}} = 0.5$ ms. Upon increasing the mixing time to 3.0 ms (Figure 4b) exchange is seen

between all three resonances. As mentioned previously, correlation times for each exchange pair were determined by measuring changes in cross-peak intensity (normalized to the sum of the intensities of the diagonal peaks) as a function of mixing time (Figure 5). By fitting this data to a first-order exponential function, correlation times, τ_c , and jump rates (k) were extracted. It should be noted that the lowest-temperature data set (283 K) for the AB exchange pair showed such low mobility that no plateau in the cross peak build-up was observed prior to the onset of T_1 relaxation. This data set therefore carries a considerably larger error from the exponential fit into the Arrhenius analysis. The jump rates from multiple integrations were averaged and error determined at the 95% confidence level. This error was insignificant as compared to the error from the first-order exponential fit and therefore this latter error was propagated into the Arrhenius analysis.

Determination of jump rates for each exchange pair at different temperatures allowed for the calculation of activation energies, E_a , by plotting $\ln k$ as a function of $1000/T$ in an Arrhenius analysis (Figure 6, top). Because of the dynamic limitations within this material, the range of temperatures for the exchange experiments was limited. At temperatures below 283 K, the dynamics were too slow for a sufficient buildup curve to be attained within the limits of the T_1 times. At higher temperatures, the three resonances began to coalesce because of fast mobility, making accurate integration of the cross-peaks difficult. Exchange between sites AC and BC is the most energetically favorable, having activation energies of $0.63 (\pm 0.03)$ eV and $0.59 (\pm 0.05)$ eV, respectively. These activation energies are comparable to bulk conductivity data acquired using impedance spectroscopy, where the activation energies were found to be 0.7 ± 0.1 eV for both $\text{Li}_3\text{V}_2(\text{PO}_4)_3$ and $\text{Li}_3\text{Fe}_2(\text{PO}_4)_3$. This is consistent with literature results

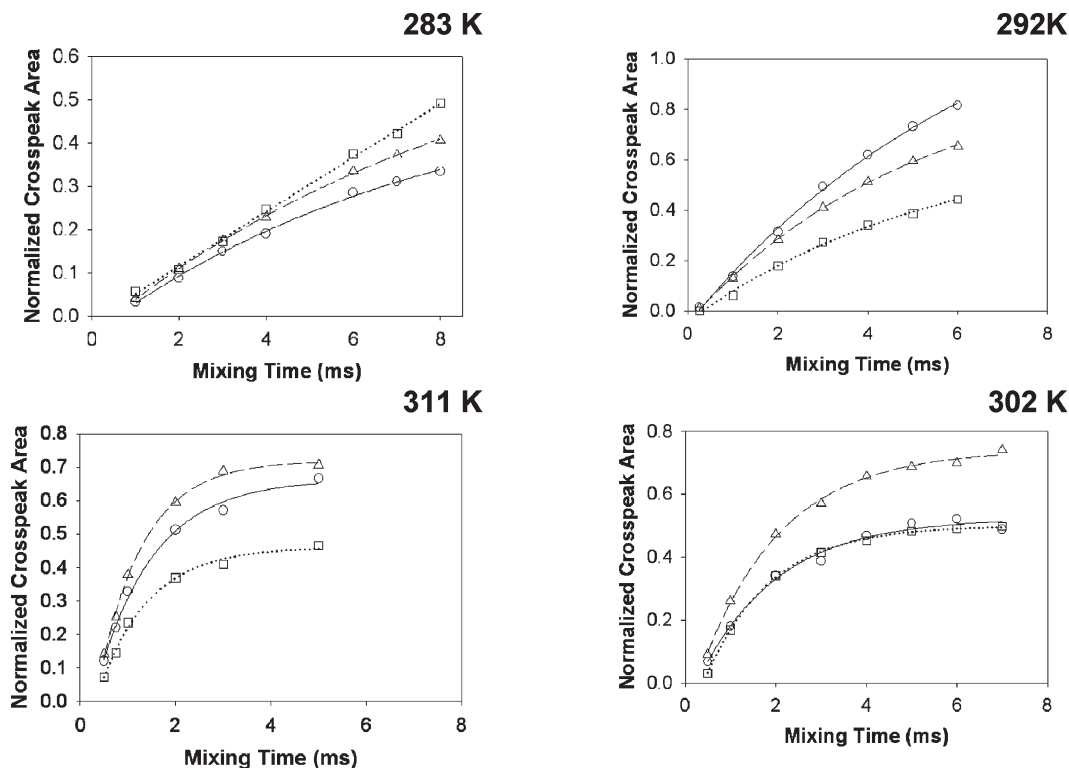


Figure 5. Normalized cross peak volume as a function of mixing time for exchange pair AB (\square), BC (\circ), and AC (\triangle) for $\text{Li}_3\text{Fe}_2(\text{PO}_4)_3$. Clockwise from top left acquisition temperatures for each data set are 283, 292, 302, and 311 K. Because of T_1 limitations, plateaus for lower-temperature data sets were not achieved.

for the lithium vanadium phosphate^{24–26} and confirms that the microscopically determined activation energies are representative of lithium-ion transport through the bulk material.

Errors for the E_a values obtained from the 2D EXSY data were calculated from the standard error of the slope from the regression analysis. When evaluated within error, the energy barriers for the AC and BC exchange pairs are equivalent and consistent, with both Li1–Li3 (BC) and Li2–Li3 (AC) having the shortest internuclear distances (3.145(0) and 3.117(6) Å, respectively; Table 2). The AB exchange pair, however, which was assigned to Li1–Li2, shows the highest energy barrier for hopping (1.3 ± 0.1 eV). This is consistent with this pair having the longest internuclear distance (Li1–Li2 3.426(2) Å). As mentioned previously, the error for the lowest-temperature jump rate (283 K) of the AB exchange pair carries a substantial error from the exponential fit of the buildup curve. This is the cause of the poor linear fit in the Arrhenius analysis and significantly larger error value on the energy barrier. To confirm whether the E_a value is highest for the longest internuclear distance, we determined the energy barrier with the AB 283 K data point set to the uppermost limit of the jump rate error bar. This gave a more accurate linear fit but more importantly, the activation energy is still considerably higher than the other two exchange pairs

(AB 0.81 ± 0.04 eV), and consistent with the bulk conductivity measurements.

When the Li–O bottlenecks for diffusion are taken into consideration, the above assignment is further confirmed (Table 2). Bottlenecks were defined as the area created by O vertices of PO_4 and FeO_6 polyhedra that were found along the pathway of a Li–Li exchange pair.¹¹ The largest bottleneck for diffusion was seen for the Li3–Li2 exchange pathway (4.22 \AA^2) (Figure 7). Alternatively, the smallest bottleneck of diffusion (3.62 \AA^2) was calculated for the Li1–Li2 diffusion channel that had been assigned to the AB exchange pair with the highest activation energy. The intermediate diffusion channel size of 3.96 \AA^2 fits with the Li1–Li3 exchange pathway and observed activation energy for the BC exchange pair.

These results are similar to those observed for the $\text{Li}_3\text{V}_2(\text{PO}_4)_3$ compound where larger activation energies are seen for exchange pairs with longer Li–Li internuclear distances and tighter bottlenecks for diffusion (Table 3).⁸ The $\text{Li}_3\text{Fe}_2(\text{PO}_4)_3$ study, however, does show smaller activation energies for all exchange pairs overall. Reasons for this difference may lie in the distribution of bottleneck sizes, where overall the bottlenecks for $\text{Li}_3\text{Fe}_2(\text{PO}_4)_3$ are more open, thus making exchange more favorable, and contributing to enhanced long-range lithium-ion transport.

Correlation of this exchange information to the available electrochemical data is underway. Although our study shows that the dynamics in the parent $\text{Li}_3\text{Fe}_2(\text{PO}_4)_3$ compound are more energetically favorable than in the parent $\text{Li}_3\text{V}_2(\text{PO}_4)_3$ material, overall the Fe

(25) Cahill, L. S. Solid-State NMR Studies of Lithium Ion dynamics in Cathode Materials for Lithium Ion Batteries. Thesis, McMaster University, Hamilton, ON, 2008.

(26) Sato, M.; Ohkawa, H.; Yoshida, K.; Saito, M.; Uematsu, K.; Toda, K. *Solid State Ionics* 2000, 135, 137–142.

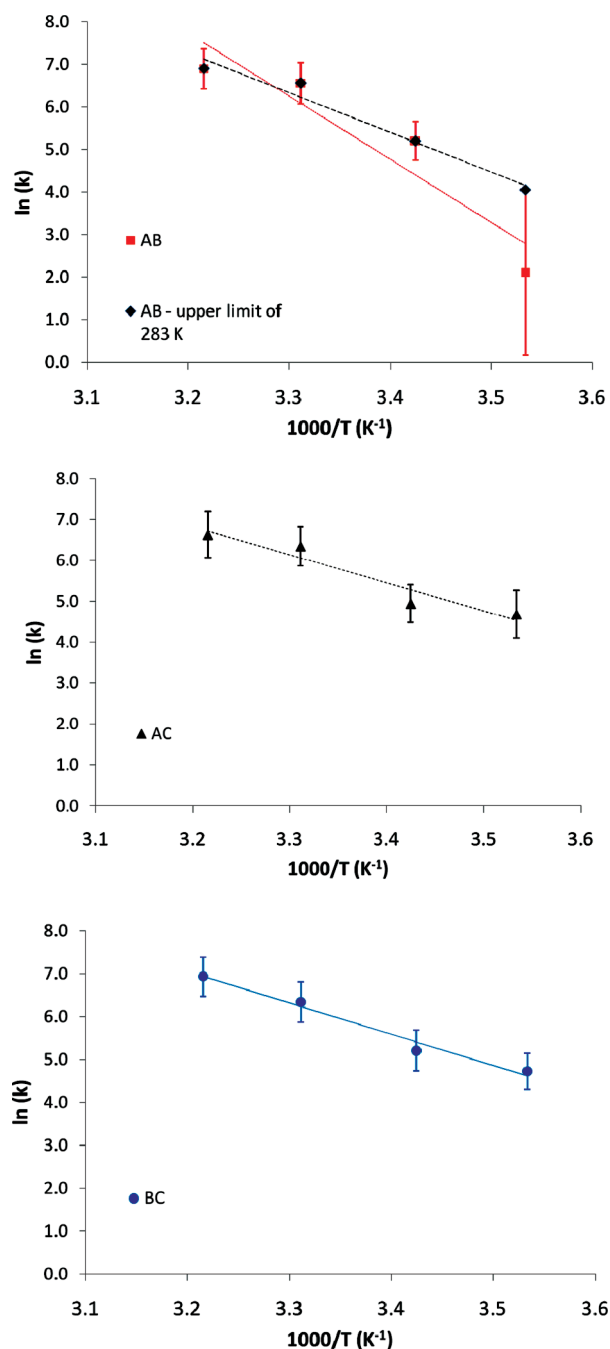


Figure 6. Arrhenius analysis for determination of activation energies for Li–Li hopping between exchange pairs AB (red squares (top)), AC (black triangles (middle)), and BC (blue circles (bottom)). For the AB exchange pair (top), the large error bar of the lowest temperature data point (283 K) obscures the fit significantly. The analysis was therefore performed with the 283 K data point set to the uppermost limit of the error bar to yield a better linear fit (black diamonds with dashed linear fit (top)). The activation barrier calculated from this analysis is closer to the value determined by bulk conductivity measurements.

intercalation cathode is not as interesting from a commercial standpoint as the vanadium analogue. Not only does $\text{Li}_3\text{V}_2(\text{PO}_4)_3$ have an overall higher operating potential with three reversible voltage plateaus²⁷ of 3.59, 3.67, and 4.06 V but it also has one of the highest

Table 2. Summary of Activation Energy Values for the Three Li–Li Exchange Pairs As Well As the Calculated Li–O Bottlenecks of Diffusion for $\text{Li}_3\text{Fe}_2(\text{PO}_4)_3$

NMR sites	Li site	E_a (eV)	Li–O bottleneck (\AA^2)	Li–Li distance (\AA)
AB	Li2–Li1	0.81 ± 0.04	3.61	3.426(2)
BC	Li1–Li3	0.59 ± 0.05	3.96	3.145(0)
AC	Li2–Li3	0.63 ± 0.03	4.22	3.117(6)

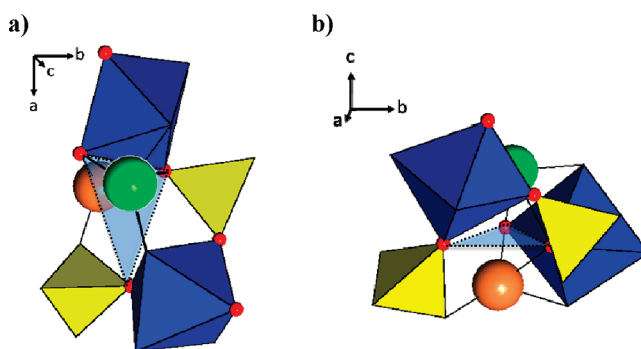


Figure 7. Schematic showing the bottleneck area created by the O atoms (gray triangles) for the Li3–Li2 exchange pair. The area of this triangle was used to quantify the Li–O bottleneck of diffusion for each exchange pair. Exchange for Li3 (orange sphere) and Li2 (green sphere) looking down (a) the c -axis and (b) the a -axis.

Table 3. Summary of Activation Energy Values for the Three Li–Li Exchange Pairs As Well As the Calculated Li–O bottlenecks of Diffusion for $\text{Li}_3\text{V}_2(\text{PO}_4)_3$

NMR sites	Li site	E_a (eV) ⁸	Li–O bottleneck (\AA^2)	Li–Li distance (\AA)
BC	Li1–Li2	0.83 ± 0.01	3.69	3.43(3)
AC	Li3–Li2	0.79 ± 0.01	3.79	3.28(3)
AB	Li3–Li1	0.73 ± 0.01	4.10	3.08(3)

theoretical capacities of all the phosphates (about 197 mA h/g).²⁸ The full capacity in fact was achieved experimentally through carbon coating of the particles.²⁹ In the case of $\text{Li}_3\text{V}_2(\text{PO}_4)_3$, results from the 2D EXSY study correlated well to the order in which the Li ions are extracted from the parent material. In the case of $\text{Li}_3\text{Fe}_2(\text{PO}_4)_3$, the high potential of the $\text{Fe}^{3+}/\text{Fe}^{2+}$ redox pair lies far outside the operating range of a typical Li-ion battery meaning that extraction of Li1, Li2, and Li3 from the iron material studied here is not possible for electrochemical applications. Instead, electrochemists exploit the $\text{Fe}^{3+}/\text{Fe}^{2+}$ redox pair through insertion of fourth and fifth lithium ions into the structure, giving two voltage plateaus at 2.65 and 2.85 V.⁵ Therefore, a direct correlation of the activation energies for ion hopping in the parent material to electrochemical extraction of lithium is not possible for the $\text{Li}_3\text{Fe}_2(\text{PO}_4)_3$. Rather, we anticipate significant changes in local lithium dynamics upon chemical or electrochemical insertion of excess lithium.

(28) Morgan, D.; Ceder, G.; Saidi, M. Y.; Barker, J.; Swayer, J.; Huang, H.; Adamson, G. *Chem. Mater.* **2002**, *14*, 4684–4693.

(29) Huang, H.; Yin, S. C.; Kerr, T.; Taylor, N.; Nazar, L. F. *Adv. Mater.* **2002**, *14*, 1525.

(27) Patoux, S.; Wurm, C.; Morcrette, M.; Rousse, G.; Masquelier, C. *J. Power Sources* **2003**, *119*–121, 278–284.

Conclusions

This work presents the first study of Li^+ dynamics in monoclinic $\text{Li}_3\text{Fe}_2(\text{PO}_4)_3$. Exchange between the crystallographic Li sites was found to be on the millisecond time scale. By plotting the change in jump rate as a function of temperature the activation barriers for Li-ion exchange were determined. The activation energies, ranging from $0.59 (\pm 0.05)$ to $0.81 (\pm 0.04)$ eV, correlated well to Li–Li internuclear distances as well as the Li–O bottlenecks along the diffusion pathway. This behavior was compared to that of $\text{Li}_3\text{V}_2(\text{PO}_4)_3$. Both materials follow the same trend of increased activation energy with decreased

bottleneck size and increased Li–Li internuclear distance. Moreover, a lower overall energy barrier for lithium dynamics in $\text{Li}_3\text{Fe}_2(\text{PO}_4)_3$ was observed. This is attributed to the observed larger bottlenecks for diffusion in this compound, and provides a direct correlation between structure and function, indicating that subtle changes in the free volume of the frameworks facilitate lithium ion mobility, on the local and macroscopic levels. $\text{Li}_3\text{Fe}_2(\text{PO}_4)_3$ and $\text{Li}_3\text{V}_2(\text{PO}_4)_3$ are candidate cathode materials for application to Li-ion batteries, thus an extensive knowledge of the dynamics of the mobile ions provides valuable insight into observed electrochemical behavior.